

Thermal Properties of A Solar Coronal Cavity Observed with the X-ray Telescope on Hinode

Katharine K. Reeves

*Harvard-Smithsonian Center for Astrophysics, 60 Garden St. MS 58, Cambridge, MA
02138*

kreeves@cfa.harvard.edu

Sarah E. Gibson

HAO/NCAR, P.O. Box 3000, Boulder, CO 80307-3000, USA

Therese A. Kucera

NASA Goddard Space Flight Center, Code 671, Greenbelt, MD 20771, USA

Hugh S. Hudson

*Space Sciences Laboratories, University of California, Berkeley, 7 Gauss Way, Berkeley,
CA, 94720*

School of Physics and Astronomy, University of Glasgow, Glasgow G12 8QQ, UK

Ryouhei Kano

National Astronomical Observatory of Japan, 2-21-1 Osawa, Mitaka, Tokyo 181-8588

ABSTRACT

Coronal cavities are voids in coronal emission often observed above high latitude filament channels. Sometimes, these cavities have areas of bright X-ray emission in their centers. In this study, we use data from the X-ray Telescope (XRT) on the *Hinode* satellite to examine the thermal emission properties of a cavity observed during July 2008 that contains bright X-ray emission in its center. Using ratios of XRT filters, we find evidence for elevated temperatures in the cavity center. The area of elevated temperature evolves from a ring-shaped structure at the beginning of the observation, to an elongated structure two days later, finally appearing as a compact round source four days after the initial observation. We use a morphological model to fit the cavity emission, and find that a uniform structure running through the cavity does not fit the observations

well. Instead, the observations are reproduced by modeling several short cylindrical cavity “cores” with different parameters on different days. These changing core parameters may be due to some observed activity heating different parts of the cavity core at different times. We find that core temperatures of 1.75 MK, 1.7 MK and 2.0 MK (for July 19, July 21 and July 23, respectively) in the model lead to structures that are consistent with the data, and that line-of-sight effects serve to lower the effective temperature derived from the filter ratio.

Subject headings: sun: prominences, sun: corona

1. Introduction

A large-scale coronal structure, the filament cavity (Vaiana et al. 1973), typically surrounds a quiescent prominence, and an analog appears as the cavity in the common three-part structure of a coronal mass ejection (CME; Illing & Hundhausen 1985). We now recognize such structures as basic building blocks of the coronal magnetic field and an important part of the development of solar activity.

The thermodynamics of coronal cavities has been studied in a variety of ways. Hudson et al. (1999); Hudson & Schwenn (2000) studied bright cavity cores in X-rays and concluded from filter ratios that these cores are hotter than their surroundings. Recently, tomographic reconstructions have been done on data sets including coronal cavities (Vázquez et al. 2009, 2010), and these studies find that the local differential emission measure distribution is hotter and broader inside cavities than in the surrounding helmet streamer. Eclipse observations have also provided thermodynamic information about cavities. Habbal et al. (2010) observed several cavities during the eclipses of 2006 March 28 and 2008 August 1 in filters centered at Fe x 637.4 nm, Fe XI 789.2 nm, Fe XII 1074.7 nm, and Fe XIV 530.3 nm, and found the cool prominences tend to be shrouded in hot material.

One possible theoretical explanation for the bright X-ray core observed by Hudson et al. (1999) is that it is due to heating along a current sheet formed at a bald-patch separatrix surface (Fan & Gibson 2006). This surface can form a sheath or tunnel enclosing the dipped prominence field lines, and would appear to be central to the cavity when viewed end on.

Another possible explanation for hot cavity cores comes from modeling the thermodynamics of dipped magnetic field lines themselves. The thermal non-equilibrium model of prominences (e.g. Karpen et al. 2003, 2005; Luna et al. 2011) postulates that prominences are cool condensations that form in dipped field lines, and predicts that the non-dipped parts of the field lines must be hot. A similar phenomenon was also seen in the calculations

of Lionello et al. (2002). These field lines are shaped such that the non-dipped portions of the loops would protrude into the cavity center when viewed edge on. This idea and the bald-patch picture are not necessarily mutually exclusive.

One problem inherent in interpreting observations of coronal cavities is that they are extended structures, and line-of-sight effects can be important. Several authors have tackled this problem by employing a morphological model of the cavity as an extended shape that wraps around the sun, and forward-modeling the relevant observables (Fuller et al. 2008; Gibson et al. 2010; Schmit & Gibson 2011; Dove et al. 2011). The tomographic reconstructions of Vásquez et al. (2009) also disambiguate line of sight effects using continuous observations over several days. Both the forward-modeling technique and the tomographic reconstructions must assume that the cavity structure remains static.

2. Observations

During the summer of 2008, a stable coronal cavity associated with a southern polar crown filament was observed by the X-ray Telescope (XRT; Golub et al. 2007) on the *Hinode* satellite (Kosugi et al. 2007). Figure 1 shows full-sun images from XRT and the Extreme ultraviolet Imaging Telescope (EIT; Delaboudinière et al. 1995) on the *Solar and Heliospheric Observatory (SoHO)* that include the cavity as it appeared on 2008 July 21.

From July 19–23, XRT observed this cavity for 8–20 hours per day using the Al-poly, Ti-poly and Thin-Be filters. The exposure times for these filters during this observation are 11.6, 16.4 and 65.5 seconds, respectively. The field of view of the observation is $\sim 790'' \times 790''$, and the images are binned 2×2 , giving a resolution of $2.0572''$ per pixel.

During the time period when XRT was observing the cavity, bright features were observed in the Thin-Be filter in the core of the cavity. Figure 2 shows the XRT Ti-poly and Thin-Be observations for several dates, as well as an EIT 304 Å image for each cavity observation. The XRT images have been averaged over an hour to increase the signal-to-noise ratio, and the color tables for the XRT images have been reversed in Figure 2, so darker colors indicate brighter intensity

For the observation on 2008 July 19 (top row of Figure 2), a bright, ring-like structure is clearly seen in the XRT Thin-Be image. The EIT 304 Å image shows a very small prominence near the location of the bright emission in the XRT images. The ellipse on the Thin-Be image indicates the cavity boundary as determined from the XRT Al-poly images, where the cavity is most visible. The bright emission in the cavity core lies well inside the cavity boundary.

The bright ring structure persists in the Thin-Be filter for several hours, until the XRT observations end at 22:45 UT on July 19. When the XRT observations resume at 10:54 UT on July 20, there is still bright emission seen at the cavity center in the Thin-Be filter, but it no longer has the coherent ring structure present in the earlier images.

The second row of Figure 2 shows the XRT Ti-poly and Thin-Be observations of the cavity on 2008 July 21. By this time the emission in the Thin-Be filter is no longer ring-like, but it is elongated parallel to the limb. This elongated structure persists until XRT stops taking data at 13:58 UT on July 22. No major prominence is seen in the EIT 304 Å image taken on at 19:19 UT on July 21, but there is a tiny prominence located further poleward than the small prominence seen on July 19.

The bottom row of Figure 2 shows the same emission images for July 23. These images are characteristic of the XRT emission from 19 UT on 22 July until the end of the observation late in the day on 23 July. The Thin-Be emission during this time period is more compact and round in shape, similar to the emission seen on 19 July, but without the ring shape.

3. Temperature and Emission Measure Measurements

We estimate the temperature and emission measure of the cavity and its surroundings using XRT filter ratios. This method is less sophisticated than tomographic reconstructions (e.g. Vásquez et al. 2009) or techniques that use multiple filters to calculate DEMs (e.g. Schmelz et al. 2010; Testa et al. 2011) in that it assumes an isothermal plasma along the line of sight. However, the filter-ratio technique is simple to apply, and it does not require days-long full-sun data sets, like the tomographic reconstruction, or data sets of more than two filters, like the DEM method. Since our data set consists of partial field-of-view images of three different filters, we can use the filter-ratio method to determine where the plasma is relatively hot, and where it is cool. Because of the isothermal assumption, we cannot determine the temperature exactly, since there is likely to be plasma at different temperatures lying along the line of sight. We will model the effects of structures lying along the line of sight in the next section.

Figure 3 shows the ratio of filter intensity as a function of temperature for the Thin-Be/Ti-poly filters and the Thin-Be/Al-poly filters. The third possible ratio for this data set, Ti-poly/Al-poly, is double-valued within the temperature range of interest, so we do not use it. There is a time-dependent contamination layer on the XRT CCD (for details, see Narukage et al. 2011), and we take this contamination into account when we calculate the observed filter ratios. The ratios shown in Figure 3 are calculated using the assumed

contamination on 2008 July 19 at 15:00 UT, but the CCD contamination does not change rapidly with time, so the ratios for later dates (i.e. July 23) are similar.

The temperature and emission measure are calculated using the `xrt_teem` routine in the SolarSoft tree. In order to create these maps, we average an hour’s worth of data in each filter to increase the signal-to-noise ratio. Errors are also calculated using `xrt_teem`. Emission measure and temperature maps created using the Thin-Be/Ti-poly ratio are shown in Figure 4 for several times during the 2008 July cavity observing run. On all three days, a temperature enhancement is seen in the core of the cavity.

For the 2008 July 19 map, a clear ring-shaped temperature enhancement is seen above the limb. This feature corresponds with the intensity enhancement seen in the Thin-Be filter, shown in Figure 2. Over the course of the next few days, this temperature enhancement evolves from the ring-like structure on July 19 to an elongated blob on July 21 to a circular structure on July 23.

Figure 4 also shows plots of the emission measure and temperature along a radial cut at 0.106 solar radii above the limb. The temperature and emission measure calculated from both the Thin-Be/Ti-poly and the Thin-Be/Al-poly filter ratios are shown. These quantities are in good agreement for the two different calculations. For simplicity, we show only the error bars from the Thin-Be/Ti-poly ratio since the error bars from the Thin-Be/Al-poly ratio are similar.

The radial cuts in temperature show that the maximum temperature enhancement in the ring-like structure in the July 19 temperature map is about 1.65 MK, and the cavity core stays between about 1.6 MK and 1.7 MK as it undergoes a morphological evolution over the next several days. The emission measure cuts show that the cavity is depleted in the center, as most cavities are (Gibson et al. 2006; Fuller & Gibson 2009), and the decrease in emission measure coincides with the increase in temperature as the cut traverses the cavity.

Scattered light in the telescope could effect the measured intensities in the XRT filters, thus skewing the temperature values derived by the filter ratio. Kano et al. (2008) used eclipse measurements to quantify the amount of scattered light off of the limb in XRT images. They found that the scattered light above the limb was very low when there were no active regions on the disk. In the observations presented here, there is a very small bright region near disk center. Another possible source of scattered light is the nearby bright limb. The scattered light in XRT due to the X-ray optics falls off as r^{-2} , where r is the distance from a bright source. In this case, the bright region on the disk is about $780''$ away, reducing any scattered light from this region to about 2×10^{-4} percent of its intensity. Likewise, the bright limb is about $100''$ away from the core of the cavity, and scattered light from this

region would thus be about 10^{-2} percent of the limb intensity. The bright region on disk and the brightest limb point are both about 300 DN in the Ti/poly filter, while the cavity core is about 20 DN. There are no synoptics including the Thin-Be filter, so the relative intensity of the bright region in this filter cannot be determined, but the magnitude of the limb intensity is similar to the cavity core in this filter. Thus the scattered light from these two regions should not be a significant factor in determining the temperature.

4. Morphological Cavity Model

In order to understand the effects of structures along the line of sight in the images, we model the observed cavity using the model presented in Gibson et al. (2010). In this model, the cavity is embedded in a helmet streamer, and makes a croissant-shaped tunnel through the streamer. We have modified this model by adding separate parameters for a bright core in the cavity center. A schematic of the model, both from the top and from the side, is shown in Figure 5.

In order to determine the model parameters that describe the morphology of the cavity and core, we first fit a series of ellipses to the cavity visible in the XRT Al-poly data between July 18 and July 23. Some of the ellipses used are shown in Figure 2. We use the Al-poly data because it shows the cavity the best out of the XRT filters. As detailed in Gibson et al. (2010), these ellipses will constrain the geometrical parameters of the morphological model. The geometrical parameters that we use for the streamer and cavity are shown in Table 1. The uncertainties given in Table 1 reflect how well a Gaussian profile can be fit to the observed ellipses.

As in Gibson et al. (2010), we use the spherically symmetric coronal hole background density defined by Guhathakurta et al. (1999) for the background radial density. For the streamer density, we use a model similar to that of Gibson et al. (1999), given by

$$N = (ar^{-b} + cr^{-d} + er^{-f}) \times 10^8 \text{ cm}^{-3}. \quad (1)$$

In our case, we use $a = 1.0$, $b = 10.3$, $c = .99$, $d = 6.34$, $e = .365$, and $f = 2.31$. This profile has an a lower initial density than that of Gibson et al. (1999), but the density falloff is similar at heights greater than about $1.2R_{\odot}$, and this profile leads to better fits between the simulated and observed X-ray images. For the cavity, the radial density falloff follows the streamer falloff, but it is depleted by 65%. For the temperature of the cavity structure, we assume an isothermal corona, but assign different temperatures to the cavity, rim, and core.

In order to determine the parameters for the bright core, we compare the modeled

intensity with the XRT Thin-Be images, where the core is most visible. To model the intensity, we take the temperature, density and geometry of the model cavity and calculate the emission using the equation

$$I = \int n_e^2(l) f_i(T(l), n_e(l)) dl \quad (2)$$

where I is the intensity observed in the telescope in units of DN s⁻¹, n_e is the electron density, $f_i(T, n)$ is a function that takes into account the atomic physics and response function of the appropriate XRT filter, and the integral is done along the line of sight, l .

We find that the best fit to the data is generated by assuming a core in the shape of a cylinder embedded in the cavity. The height, width, length and other geometrical parameters of the core are varied until they best fit the data. We find that one consistent set of parameters does not fit the data on all of the days that the cavity was observed, so we use different geometrical and thermodynamic parameters for each of the three days shown in Figure 2. The parameters that we use for cores fit to each of the three days are given in Table 2, and the simulated XRT Thin-Be images are shown in Figure 6.

We find that using this model, we are not able to reproduce the bright ring of emission visible in the Thin-Be filter on July 19 (see the top row of Figure 2), so we incorporate a final geometrical parameter, which is the ability to put a hole in the core of the cavity. This “hole” takes on the same temperature and density parameters as the cavity, and its diameter is variable. In our case we use a “hole” diameter of $0.05 R_\odot$. As can be seen in the bottom left panel of Figure 6, these geometrical parameters produce a good fit to the data, and reproduce the ring structure well.

The bright emission in the Thin-Be filter on July 21 is elongated parallel to the Sun’s surface, and not a round shape like the emission on July 19 and July 23. In order to model this emission, we find that we need to rotate the emitting core at an angle of about 10° from the equator. This angle could arise from the activation of plasma in a substructure off of the main filament channel, as shown schematically in Figure 7. The simulated emission for July 21 is shown in the bottom middle panel of Figure 6. Although it is difficult to reproduce the fine details of the structure observed on July 21, the general shape of the bright emission in the Thin-Be filter is well captured.

The emission on July 23 is well-modeled by a compact, round source, lying at the same angle to the equator as the cavity. For this observation, the data are best fit by a relatively hot cavity core, at 2.0 MK. The simulated image for this date is shown in the bottom right panel of Figure 6.

We create temperature and emission measure maps from the model by first simulating

the intensity of the Ti-poly and Thin-Be filters using Equation 2. The synthetic intensities are then processed in the same manner as the data, using `xrt_teem`, to produce synthetic emission measure and temperature maps. These maps are shown in Figure 8 for an Earth-centered observing point. A plot of a radial cut of the simulated temperature and emission measure at 0.106 solar radii above the limb is also shown, for easy comparison with the data. The ring-shaped temperature enhancement observed in the core of the cavity on July 19 is well reproduced by the model. The density depletion is not as pronounced as in the data for this date, possibly because of intervening foreground structures in the observations that are not accounted for in the model. Temperature enhancement parallel to the limb on July 21 is also well reproduced by the model, as is the compact region of hotter temperatures on July 23.

The longitudinal extension of the model cavity and core structure necessitates that plasma at different temperatures along the line of sight contribute to the filter ratio and the derived temperature. Since we know the input temperatures in the model, we can compare the real temperatures to those derived through the ratio method. For both the 19 July and 23 July models, the filter-ratio temperature in the cavity core is less than the model core temperature by about 10%, due to the line-of-sight effects. The maximum filter ratio temperature in the center of the core in the July 21 model is similar to the model core temperature, but there is a falloff of the filter ratio temperature outside of the core center.

5. Discussion and Conclusions

In previous work, we were able to find a coherent cavity structure that explained the geometry of the cavity over several days (Gibson et al. 2010). In the current research, we could not come up with one continuous structure that explains all three observations of the bright cavity core. One explanation for this situation could be that the bright core emission is intrinsically more time-varying than the cavity. There is some evidence for this conclusion in the observations. The bright cavity core emission does not show up as well in the extreme ultraviolet as it does in the X-rays, but the ratio of a 284 Å image to a 195 Å image brings out the bright core structure reasonably well. Figure 9 shows ratios of these images from the *STEREO* EUVI (Extreme UltraViolet Imager, Howard et al. 2008) corresponding to the structure seen on the limb on July 21 in XRT. Since the *STEREO* B spacecraft is behind the Earth in its orbit, EUVI B sees the structure on the limb before XRT. The *STEREO* A spacecraft is ahead of the Earth in its orbit, so EUVI A sees the structure on the limb later than XRT. These three different views of the structure on the limb at different times, but the same Carrington longitude, give an idea of how the structure

evolves with time. The bright cores structure clearly changes size and shape as time passes.

Figure 10 shows XRT Thin-Be images indicating some bright transients that appear between the observation on July 19 and the observation on July 21. In the bottom left panel, a horizontal arrow marks a bright point which emerges between 11 UT and 20 UT on July 20. Also indicated in this image are a bright loop and some bright emission along the limb. These features are probably the result of reconnections between the emerging bright point and the overlying cavity fields. In the middle panel in Figure 10, arrows mark a transient brightening that seems to stream along the filament channel. The arrows in the right panel in Figure 10 indicate another emerging bright point to the north of the cavity core. Given these dynamics, it is not surprising that the core material is not well fit by a single static structure.

The shape of the plasma in the core of the cavity, particularly the hot, bright ring-shaped structure visible on 19 July, suggests that the core plasma is associated with an interface between two different magnetic field structures within the cavity. The cylindrical core structures in the morphological model are consistent with the idea that the X-ray emission regions lie along twisted features seen more or less end-on, preferentially near the filament material. The dynamics can be explained by the fact that the filament channel and the cavity are the more long-lived robust structures, as compared to the filament which comes and goes along portions of the channel and cavity, in a manner probably associated with changes in heating and magnetic fields. If the bright cavity core plasma is indeed due to heating at the interface between the fields of the prominence and the outer cavity, it would thus be sensitive to changes in the fields (due to reconnection from emerging bright points for example), and different parts of the core would light up at different times accordingly.

The picture outlined above supports the idea that the bright X-ray emission is caused by heating on a current sheet at a separatrix surface between a prominence-loaded twisted cavity flux rope and the external sheared field that is part of the outer cavity, as suggested by Fan & Gibson (2006). Another possibility is that long, sheared strands with the thermodynamic properties described by Karpen et al. (2003) and Luna et al. (2011) are positioned along the line of sight. In this model, the hot core plasma is caused by the amalgamation along the line-of-sight of the hot coronal parts of dipped, sheared field lines that contain prominence material, and it is even possible to create apparent ring-like structures in the cavity core (Luna et al. 2011), though these structures are visible in the cooler 171 Å simulated emission.

Differentiating between these two models, and making further progress in understanding cavity thermodynamics in general, requires knowledge of the magnetic field structure inside the cavity. Promising work along these lines has recently been done by Dove et al. (2011), who find that coronal magnetic field measurements from the Coronal Multi-Channel Polarimeter

(CoMP) instrument at Mauna Loa Solar Observatory for a cavity observed on 2005 April 21 are consistent with a spheromak magnetic field configuration. Unfortunately, no CoMP data are available for the observations presented above, but the combination of coronal magnetic field data and soft X-ray and EUV imaging data will clearly be a powerful tool in understanding the magnetic structure and thermodynamics of coronal cavities.

Acknowledgements

The authors would like to thank the International Space Science Institute (ISSI) for funding a Working Group on Coronal Cavities, where this work began. K. K. Reeves is supported under contract NNM07AB07C from NASA to SAO. T. Kucera is supported by an award from the NASA SHP Program. The National Center for Atmospheric Research is sponsored by the National Science Foundation. *Hinode* is a Japanese mission developed and launched by ISAS/JAXA, with NAOJ as domestic partner and NASA and STFC (UK) as international partners. It is operated by these agencies in co-operation with ESA and NSC (Norway). *SoHO* is a project of international collaboration between ESA and NASA. The *STEREO/SECCHI* data used here are produced by an international consortium of the Naval Research Laboratory (USA), Lockheed Martin Solar and Astrophysics Lab (USA), NASA Goddard Space Flight Center (USA) Rutherford Appleton Laboratory (UK), University of Birmingham (UK), Max-Planck-Institut für Sonnensystemforschung (Germany), Centre Spatiale de Liège (Belgium), Institut d’Optique Théorique et Appliquée (France), and Institut d’Astrophysique Spatiale (France).

REFERENCES

- Delaboudinière, J.-P., Artzner, G. E., Brunaud, J., Gabriel, A. H., Hochedez, J. F., Millier, F., Song, X. Y., Au, B., Dere, K. P., Howard, R. A., Kreplin, R., Michels, D. J., Moses, J. D., Defise, J. M., Jamar, C., Rochus, P., Chauvineau, J. P., Marioge, J. P., Catura, R. C., Lemen, J. R., Shing, L., Stern, R. A., Gurman, J. B., Neupert, W. M., Maucherat, A., Clette, F., Cugnon, P., & van Dessel, E. L. 1995, *Sol. Phys.*, 162, 291
- Dove, J. B., Gibson, S. E., Rachmeler, L. A., Tomczyk, S., & Judge, P. 2011, *ApJ*, 731, L1+
- Fan, Y. & Gibson, S. E. 2006, *ApJ*, 641, L149
- Fuller, J. & Gibson, S. E. 2009, *ApJ*, 700, 1205
- Fuller, J., Gibson, S. E., de Toma, G., & Fan, Y. 2008, *ApJ*, 678, 515

- Gibson, S. E., Fludra, A., Bagenal, F., Biesecker, D., del Zanna, G., & Bromage, B. 1999, *J. Geophys. Res.*, 104, 9691
- Gibson, S. E., Foster, D., Burkepille, J., de Toma, G., & Stanger, A. 2006, *ApJ*, 641, 590
- Gibson, S. E., Kucera, T. A., Rastawicki, D., Dove, J., de Toma, G., Hao, J., Hill, S., Hudson, H. S., Marqué, C., McIntosh, P. S., Rachmeler, L., Reeves, K. K., Schmieder, B., Schmit, D. J., Seaton, D. B., Sterling, A. C., Tripathi, D., Williams, D. R., & Zhang, M. 2010, *ApJ*, 724, 1133
- Golub, L., Deluca, E., Austin, G., Bookbinder, J., Caldwell, D., Cheimets, P., Cirtain, J., Cosmo, M., Reid, P., Sette, A., Weber, M., Sakao, T., Kano, R., Shibasaki, K., Hara, H., Tsuneta, S., Kumagai, K., Tamura, T., Shimojo, M., McCracken, J., Carpenter, J., Haight, H., Siler, R., Wright, E., Tucker, J., Rutledge, H., Barbera, M., Peres, G., & Varisco, S. 2007, *Sol. Phys.*, 243, 63
- Guhathakurta, M., Fludra, A., Gibson, S. E., Biesecker, D., & Fisher, R. 1999, *J. Geophys. Res.*, 104, 9801
- Habbal, S. R., Druckmüller, M., Morgan, H., Scholl, I., Rušin, V., Daw, A., Johnson, J., & Arndt, M. 2010, *ApJ*, 719, 1362
- Howard, R. A., Moses, J. D., Vourlidas, A., Newmark, J. S., Socker, D. G., Plunkett, S. P., Korendyke, C. M., Cook, J. W., Hurley, A., Davila, J. M., Thompson, W. T., St Cyr, O. C., Mentzell, E., Mehalick, K., Lemen, J. R., Wuelser, J. P., Duncan, D. W., Tarbell, T. D., Wolfson, C. J., Moore, A., Harrison, R. A., Waltham, N. R., Lang, J., Davis, C. J., Eyles, C. J., Mapson-Menard, H., Simnett, G. M., Halain, J. P., Defise, J. M., Mazy, E., Rochus, P., Mercier, R., Ravet, M. F., Delmotte, F., Auchere, F., Delaboudiniere, J. P., Bothmer, V., Deutsch, W., Wang, D., Rich, N., Cooper, S., Stephens, V., Maahs, G., Baugh, R., McMullin, D., & Carter, T. 2008, *Space Sci. Rev.*, 136, 67
- Hudson, H. & Schwenn, R. 2000, *Advances in Space Research*, 25, 1859
- Hudson, H. S., Acton, L. W., Harvey, K. L., & McKenzie, D. E. 1999, *ApJ*, 513, L83
- Illing, R. M. E. & Hundhausen, A. J. 1985, *J. Geophys. Res.*, 90, 275
- Kano, R., Sakao, T., Hara, H., Tsuneta, S., Matsuzaki, K., Kumagai, K., Shimojo, M., Minesugi, K., Shibasaki, K., Deluca, E. E., Golub, L., Bookbinder, J., Caldwell, D., Cheimets, P., Cirtain, J., Dennis, E., Kent, T., & Weber, M. 2008, *Sol. Phys.*, 249, 263

- Karpen, J. T., Antiochos, S. K., Klimchuk, J. A., & MacNeice, P. J. 2003, *ApJ*, 593, 1187
- Karpen, J. T., Tanner, S. E. M., Antiochos, S. K., & DeVore, C. R. 2005, *ApJ*, 635, 1319
- Kosugi, T., Matsuzaki, K., Sakao, T., Shimizu, T., Sone, Y., Tachikawa, S., Hashimoto, T., Minesugi, K., Ohnishi, A., Yamada, T., Tsuneta, S., Hara, H., Ichimoto, K., Suematsu, Y., Shimojo, M., Watanabe, T., Shimada, S., Davis, J. M., Hill, L. D., Owens, J. K., Title, A. M., Culhane, J. L., Harra, L. K., Doschek, G. A., & Golub, L. 2007, *Sol. Phys.*, 243, 3
- Lionello, R., Mikić, Z., Linker, J. A., & Amari, T. 2002, *ApJ*, 581, 718
- Luna, M., Karpen, J. T., & DeVore, C. R. 2011, *ApJ*, submitted
- Narukage, N., Sakao, T., Kano, R., Hara, H., Shimojo, M., Bando, T., Urayama, F., DeLuca, E., Golub, L., Weber, M., Grigis, P., Cirtain, J., & Tsuneta, S. 2011, *Sol. Phys.*, 269, 169
- Schmelz, J. T., Saar, S. H., Nasraoui, K., Kashyap, V. L., Weber, M. A., DeLuca, E. E., & Golub, L. 2010, *ApJ*, 723, 1180
- Schmit, D. J. & Gibson, S. E. 2011, *ApJ*, 733, 1
- Testa, P., Reale, F., Landi, E., DeLuca, E. E., & Kashyap, V. 2011, *ApJ*, 728, 30
- Vaiana, G. S., Krieger, A. S., & Timothy, A. F. 1973, *Sol. Phys.*, 32, 81
- Vásquez, A. M., Frazin, R. A., & Kamalabadi, F. 2009, *Sol. Phys.*, 256, 73
- Vásquez, A. M., Frazin, R. A., & Manchester, W. B. 2010, *ApJ*, 715, 1352

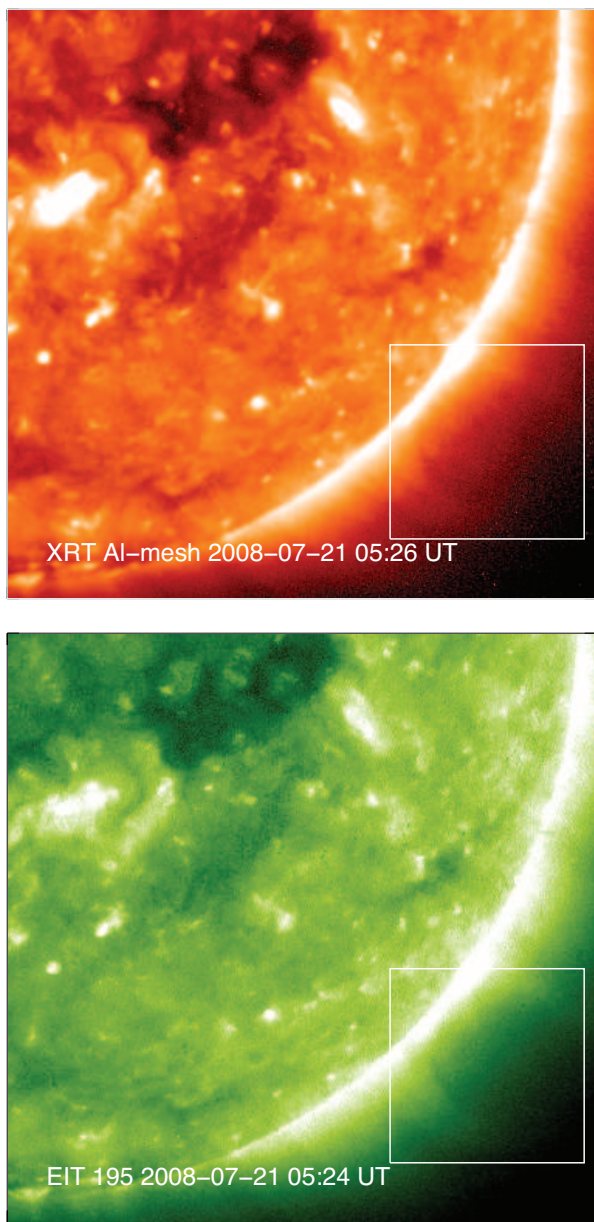


Fig. 1.— XRT Al-mesh synoptic image (top) and EIT 195 Å image (bottom) showing the cavity as it appeared on the west limb on 2008 July 21. The location of the cavity is indicated by a box.

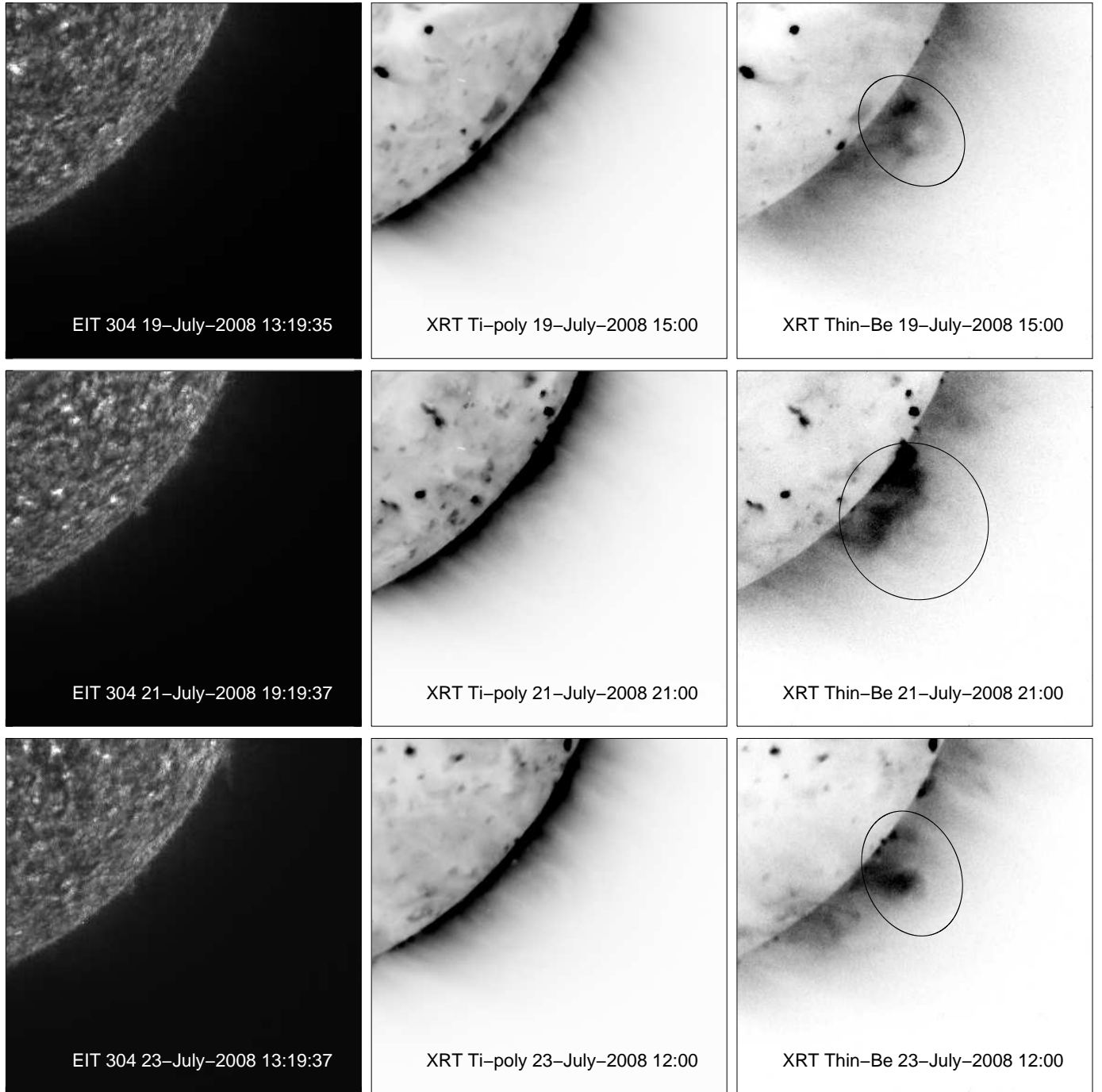


Fig. 2.— EIT 304 Å (left) and XRT Ti-poly (center) and Thin-Be (right) images for the cavity observed on 2008 July 19 (top row), 2008 July 21 (middle row), and 2008 July 23 (bottom row). The color table for the XRT images is reversed. The XRT images are averaged over an hour to increase the signal to noise ratio. The ellipses shown on the Thin-Be images are the cavity boundary as determined from the XRT Al-poly images. These ellipses are used to define the cavity geometry in the morphological model described below.

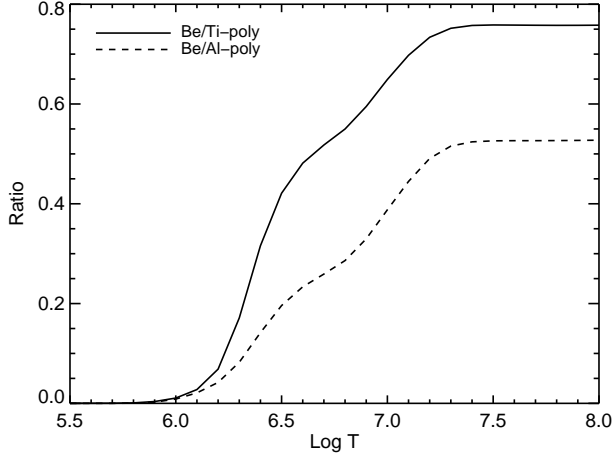


Fig. 3.— Temperature dependence of the XRT Thin-Be/Ti-poly ratio (solid line) and the Thin-Be/Al-poly ratio (dotted line).

Table 1: Geometrical parameters for the streamer and cavity in the morphological model

Quantity	Parameter	Value
Streamer central colatitude	θ_0	$131^\circ.41 \pm 3.27$
Streamer central Carrington longitude	ϕ_0	252.29 ± 0.52
Angle of streamer axis to equator	m	$2^\circ.57^a$
Tilt of streamer height axis vs. radial	α	0°
Streamer half-width at photosphere	S_{width}	40°
Streamer half-length at photosphere	S_{length}	100°
Streamer current sheet height	R_{cs}	$2.5 R_\odot$
Streamer current sheet half-width	CS_{width}	3°
Cavity top radius at ϕ_0	r_{ctop_0}	$1.33 R_\odot \pm 0.005$
Cavity top colatitude at ϕ_0	θ_{ctop_0}	$131^\circ.69 \pm 1.78$
Cavity height at ϕ_0	C_{rad_0}	$0.331 R_\odot \pm 0.005$
Cavity width at ϕ_0	C_{norm_0}	$0.296 R_\odot \pm 0.005$
Cavity half length	C_{length}	$35^\circ \pm 2$

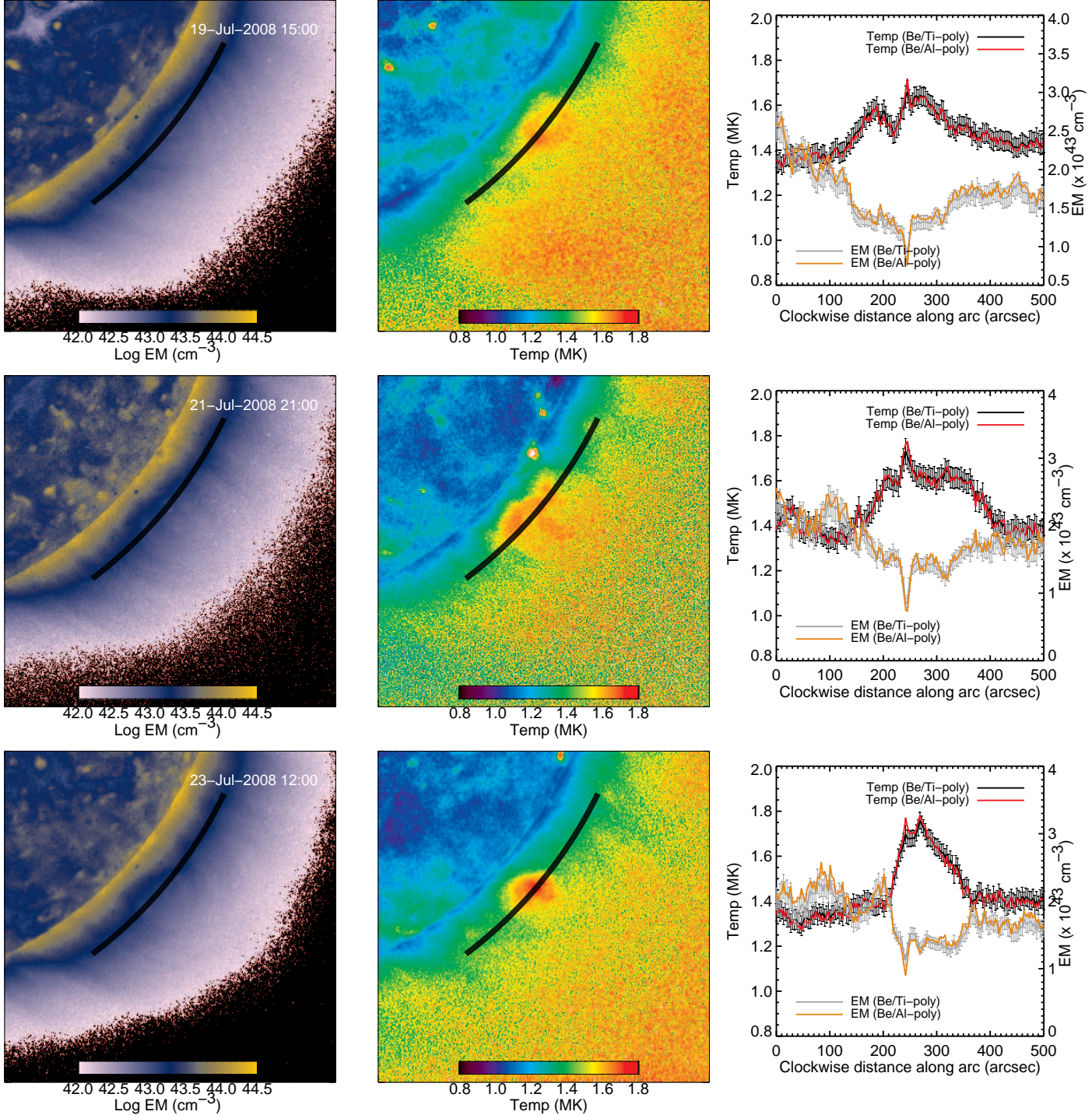


Fig. 4.— The left column shows maps of the emission measure calculated for the three dates shown in Figure 2, derived using the XRT Thin-Be/Ti-poly filter pair. The middle column shows maps of the temperature calculated for the same cavity and filter pair. The right column shows the emission measure and temperature along the arc plotted in the images using the Thin-Be/Ti-poly filter pair (gray/black) and the Thin-Be/Al-poly filter pair (orange/red). For simplicity, only the error bars calculated from the Thin-Be/Ti-poly are shown.

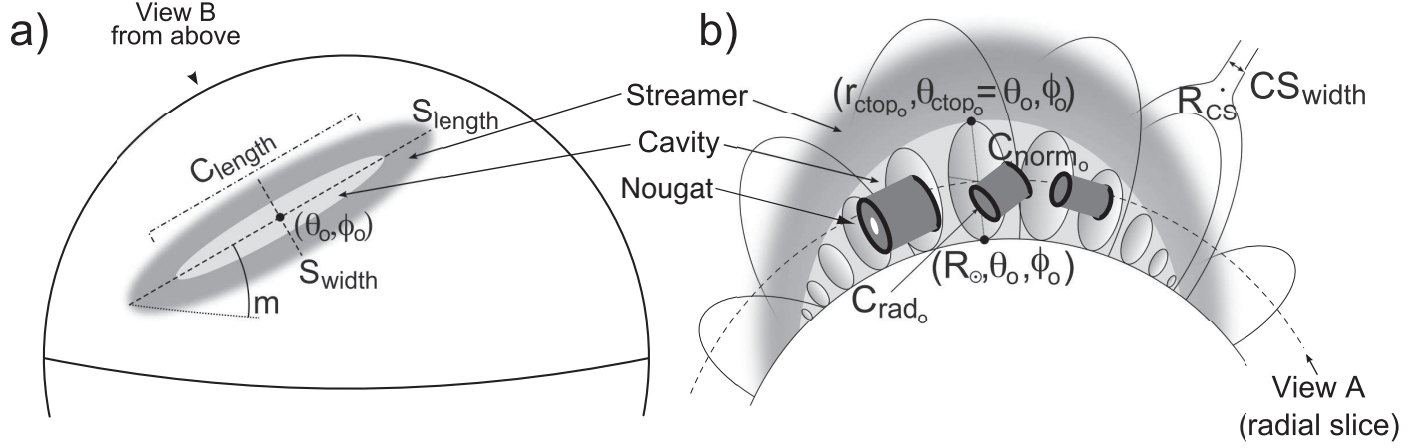


Fig. 5.— Panel (a) shows the view of the morphological model on the solar disk and panel (b) shows the view from above. Modified from Gibson et al. (2010).

Table 2: Geometrical and thermodynamic parameters for the cavity cores used in the morphological model

Quantity	Parameter	2008 Jul 19	2008 Jul 21	2008 Jul 23
Angle of core to equator	m_N	$2^\circ.57$	10°	$2^\circ.57$
Core central Carrington longitude	ϕ_N	282	242	230
Core top radius at ϕ_0	r_{Ntop_0}	$1.16 R_\odot$	$1.13 R_\odot$	$1.15 R_\odot$
Core top colatitude at ϕ_0	θ_{Ntop_0}	131.4°	131.4°	131.4°
Core height at ϕ_0	N_{rad_0}	$0.09 R_\odot$	$0.06 R_\odot$	$0.07 R_\odot$
Core width at ϕ_0	N_{norm_0}	$0.09 R_\odot$	$0.07 R_\odot$	$0.06 R_\odot$
Core half length	N_{length}	20°	20°	15°
Percent of core occupied by “hole”		30%	0%	0%
Temperature of Cavity		1.6 MK	1.65 MK	1.5 MK
Temperature of Rim		1.3 MK	1.35 MK	1.3 MK
Temperature of Core		1.75 MK	1.70 MK	2.0 MK
Core density scale factor ^a		1.2	1.8	1.2

^aThe core density is the scale factor times the cavity density.

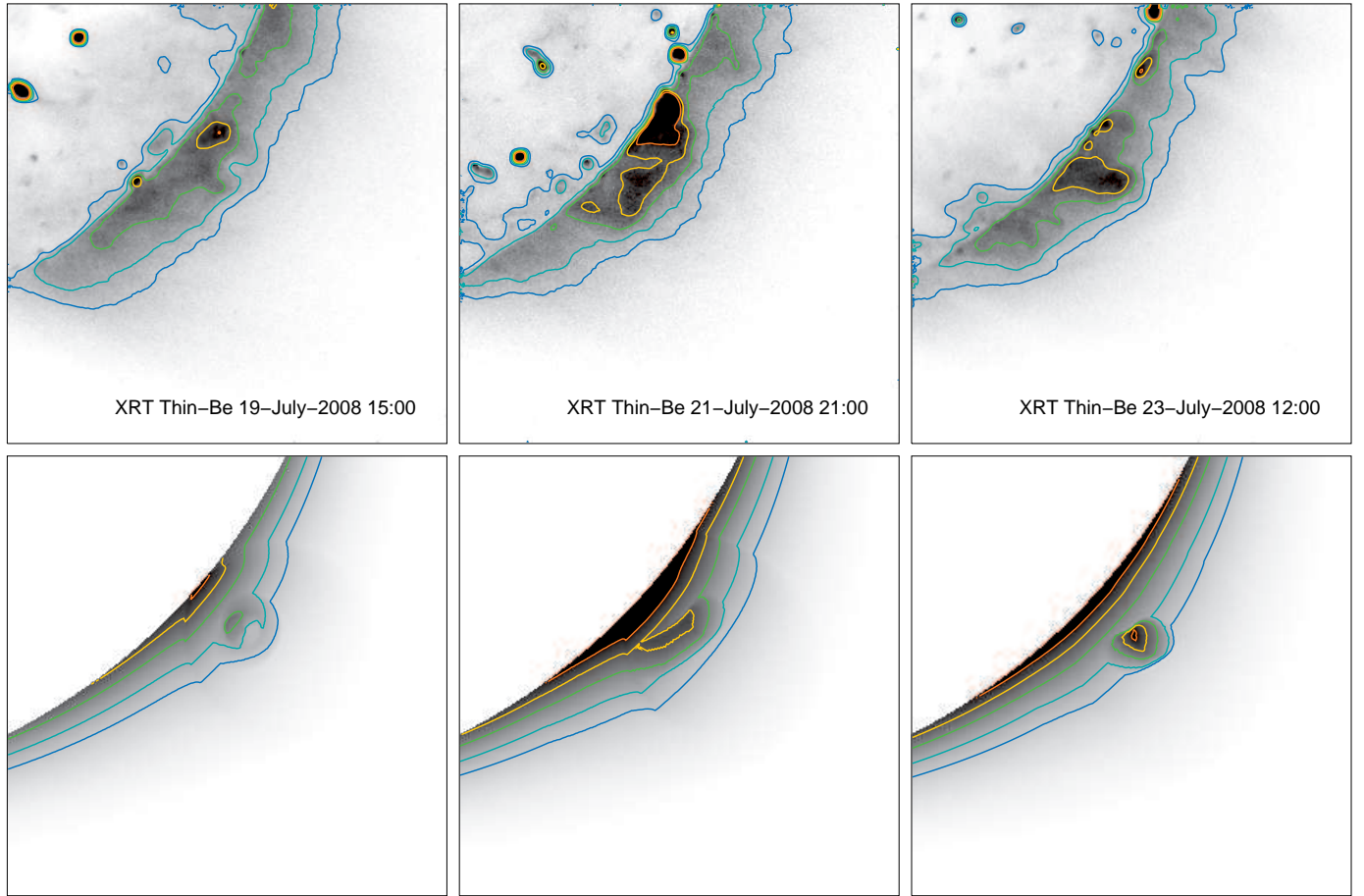


Fig. 6.— Top row: Observed Thin-Be images for the three days shown in Figure 2, with intensity contours. Bottom row: Simulated XRT Thin-Be images for the same three days with the same contours as the observed images.

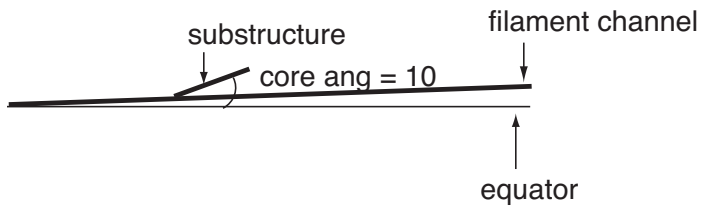


Fig. 7.— A schematic cartoon showing the filament channel and substructure that may contribute to the hot emission in the 21 July XRT images.

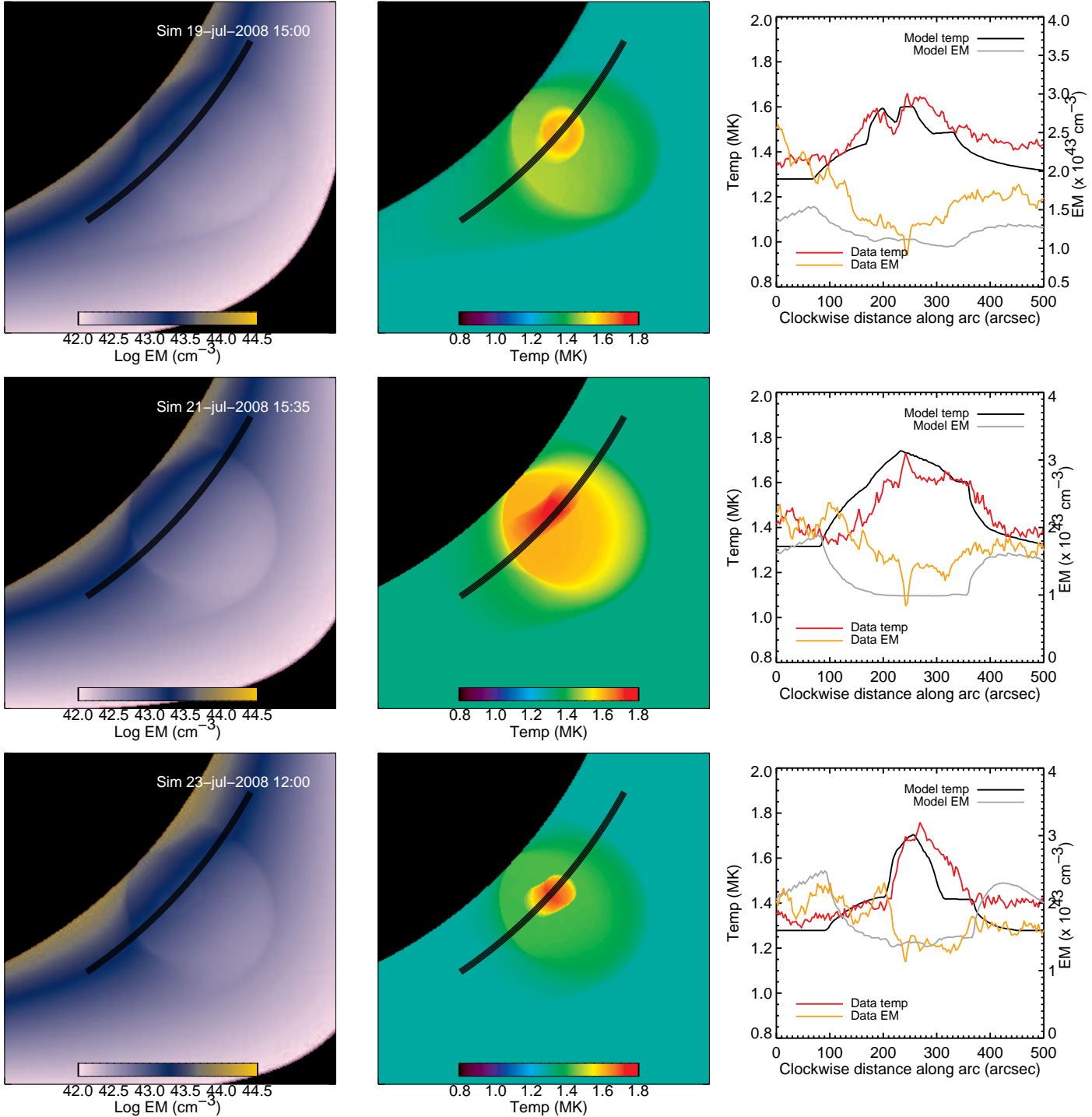


Fig. 8.— The left column shows synthetic maps of the emission measure using the morphological model with an earth-centered viewpoint for the same three days shown in Figure 4, derived using simulated XRT Thin-Be and Ti-poly filter intensities. The center column shows maps of the synthetic temperature calculated for the same model and filter pair. The right column shows the emission measure (grey) and temperature (black) along the arc plotted in the images, as well as the data for temperature (red) and emission measure (orange) from the Thin-Be/Ti-poly filter pair.



Fig. 9.— The ratio of 284 Å to 195 Å from EUVI B, EIT and EUVI A images at the the same Carrington longitude, showing the evolution over several days of the part of the cavity visible from Earth on 21 July.

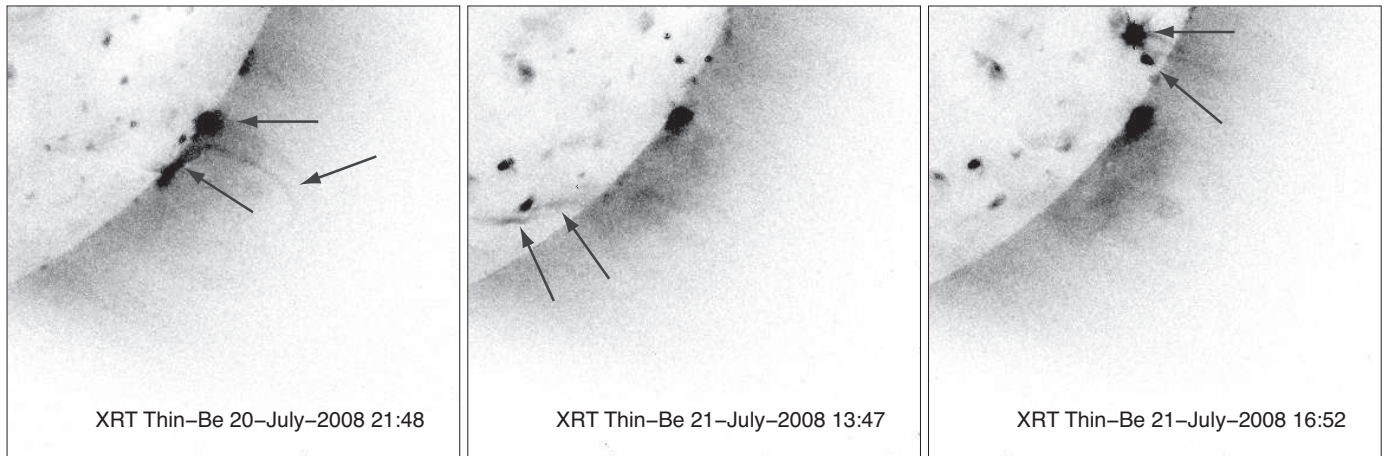


Fig. 10.— XRT Thin-Be images showing transient brightenings (marked with arrows) that occur at several times between 19 July and 21 July.